Applied Physics Letters

Magnetization reversal of $(Sm, Ce)_2(Co, Fe, Cu, Zr)_{17}$ magnets as per soft x-ray magnetic circular dichroism microscopy

Cite as: Appl. Phys. Lett. **117**, 022409 (2020); https://doi.org/10.1063/5.0005635
Submitted: 27 February 2020 . Accepted: 26 June 2020 . Published Online: 15 July 2020

Yutaka Matsuura, Ryo Maruyama, Ryo Kato, Ryuji Tamura, Keisuke Ishigami, Kazushi Sumitani, Kentaro Kajiwara, and Tetsuya Nakamura

AIP Publishing

Applied Physics Letters ARTICLE scitation.org/journal/apl

Magnetization reversal of $(Sm, Ce)_2(Co, Fe, Cu, Zr)_{17}$ magnets as per soft x-ray magnetic circular dichroism microscopy

Cite as: Appl. Phys. Lett. **117**, 022409 (2020); doi: 10.1063/5.0005635
Submitted: 27 February 2020 · Accepted: 26 June 2020 ·
Published Online: 15 July 2020

Yutaka Matsuura,[1,a)] Ryo Maruyama,[2] Ryo Kato,[2] Ryuji Tamura,[2] Keisuke Ishigami,[3] Kazushi Sumitani,[3] Kentaro Kajiwara,[3] and Tetsuya Nakamura[3,4]

AFFILIATIONS

[1]Research Institute for Applied Sciences, Kyoto 606-8202, Japan
[2]Department of Materials Science and Technology, Faculty of Industrial Science and Technology, Tokyo University of Science, Tokyo 125-8585, Japan
[3]Japan Synchrotron Radiation Research Institute, Sayo 679-5198, Japan
[4]Institute of Multidisciplinary Research for Advanced Materials (IMRAM), Tohoku University, Sendai 980-8577, Japan

[a)]**Author to whom correspondences should be addressed:** yutaka.matsuura@rias.or.jp

ABSTRACT

We investigated magnetization reversal of $(Sm, Ce)_2(Co, Fe, Cu, Zr)_{17}$ magnets as per x-ray magnetic circular dichroism microscopy. Magnetization reversal initially occurs at the ferromagnetic grain boundaries or in the vicinity of nonmagnetic Sm oxides. As the demagnetization field increases after magnetization reversal, the reversal region extends into the grain from these areas by the magnetic domain wall motion. Energy-dispersive x-ray analysis using an electron probe micro-analyzer shows that, at the grain boundaries, the Fe concentration is higher and the Cu concentration is lower compared to that inside of the grains; and concentrations of Sm, Co, Fe, and Cu vary in the vicinity of Sm oxides. By measuring the Co L_3 absorption intensity, we verified that local coercivities in these areas are very low compared to those inside of the grain. These results imply that the magnetization reversal that occurs in these areas is induced by the variation in the composition. The results obtained in our research will be useful for improving the magnetic properties of Sm–Co magnets.

Sm–Co magnets including RCo_5 and R_2Co_{17} type magnets, where R is a rare earth element, are still very important in various applications. These include automotive sensors such as anti-lock braking, high-temperature motors such as in trains and aircraft, and quadrupole field magnets used in high-energy accelerators. Sm–Co magnets were developed in the late 1960s and 1970s[1–5] and reached more than 240 kJ/m^3 of maximum energy product $[(BH)_{max}]$ in Sm_2Co_{17} type magnets.[6] These magnets show excellent magnetic performance of magnetic properties with high remanence and coercivity, where the remanence (or the residual magnetization) and coercivity are denoted by B_r and H_{cJ}, respectively. They also have high Curie temperatures and exhibit excellent heat resistance over 150 °C.

The magnetic properties of Sm_2Co_{17} magnets continue to improve. Recently, researchers reported that the magnetic properties of a Sm_2Co_{17}-type magnet, $Sm(Co_{0.572}Fe_{0.35}Cu_{0.06}Zr_{0.018})_{7.8}$, achieved a very high $(BH)_{max}$ (more than 280 kJ/m^3) by improving solution heat treatment, aging heat treatment, and optimizing the Fe content.[7,8]

In Sm_2Co_{17}-type magnets, the cellular structure (in which there is a Sm_2Co_{17} phase and a plate-like $SmCo_5$ phase enriched in Cu) forms as a result of aging heat treatment, and the magnetic domain walls are constrained by the difference in the magnetic wall energy between the aforementioned two phases.[9,10] The coercivity mechanism of these magnets has mainly been studied by investigations of the cellular structure using transmission electron microscopy. Additionally, the squareness of the demagnetization curve defined by H_k/H_{cJ}, where H_k is the magnetic field at which magnetization is 90% of Br, is less than that of Nd–Fe–B sintered magnets.

Recently, Kerr effect microscopy indicated that the origin of the grain boundaries of Sm_2Co_{17} magnets that have high squareness in the demagnetization curve pertains to the initial stage of magnetization reversal.[11–13] Knowledge of where the initial magnetization reversal

occurs and how the magnetization reversal domains develop is important to further improve magnetic properties, especially the squareness of the demagnetization curve. Toward this goal, we investigated the magnetization reversal of $(Sm, Ce)_2(Co, Fe, Cu, Zr)_{17}$ magnets using soft x-ray magnetic circular dichroism (XMCD) microscopy, which gives higher spatial resolution and a larger magnetic effect compared to Kerr microscopy.

A highly oriented Sm_2Co_{17}-type magnet with the composition of $Sm_{0.67}Ce_{0.33}(Co_{0.73}Fe_{0.2}Cu_{0.05}Zr_{0.02})_{7.2}$ was provided by Shin-Etsu Chemical Co., Ltd. The samples used for magnetic property measurements were of dimensions 7 mm × 7 mm × 7 mm. The magnetic properties were measured using a pulsed field magnetometer (TPM-2–08S25VT-C, Toei Industry Co., Ltd, Tokyo Japan). A maximum magnetic field of 8 T was applied for magnetic saturation. The hysteresis curve measured using the pulsed field magnetometer was subjected to a demagnetization correction.

XMCD microscopy was performed at the soft X-ray beamline, BL25SU, of SPring-8.[14] For these experiments, magnets were cut from a block magnet into a pillar shape with dimensions of 0.6 mm × 0.6 mm × L mm, where the easy magnetization direction is along the L-axis. This magnet was fractured perpendicular to the L-axis under high vacuum ($\sim 4.89 \times 10^{-6}$ Pa) to prevent oxidation of the cracked surface in the sub-chamber and was then transferred into the main chamber ($\sim 4.6 \times 10^{-7}$ Pa). The XMCD measurements were conducted at room temperature with an external magnetic field (H) as follows: $-5.0\ \mathrm{T} \leq H \leq +5.0\ \mathrm{T}$. The measurements were performed on a surface perpendicular to the easy magnetization direction. The incident x-rays and external magnetic field were parallel to the easy magnetization direction. The measurement area was 55.95 μm × 60.00 μm, and the scanning step was 150 nm.

X-ray absorption intensity was measured using the total electron yield at the Co L_3 pre-edge (774.0 eV), Co L_3 edge (778.5 eV), Sm M_5 pre-edge (1066.0 eV), and Sm M_5 edge (1078.6 eV). In these energy regions, the x-ray beam was focused to approximately 100 nm × 100 nm, and the focal depth was approximately ±5 μm. The probing depth was 1.5 nm. The XMCD ratio was determined by the ratio of the difference to the sum (referring to the absorption intensities attributable to positive and negative photon helicity). The XMCD ratio and its map were used to observe local magnetic properties and magnetization reversal, respectively. David Billington *et al.* describe the XMCD microscopy measurement method in more detail.[15]

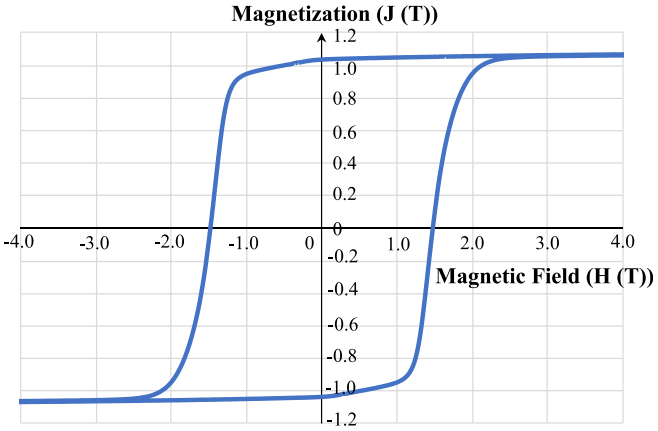

FIG. 1. Hysteresis curve of $Sm_{0.67}Ce_{0.33}(Co_{0.73}Fe_{0.2}Cu_{0.05}Zr_{0.02})_{7.2}$.

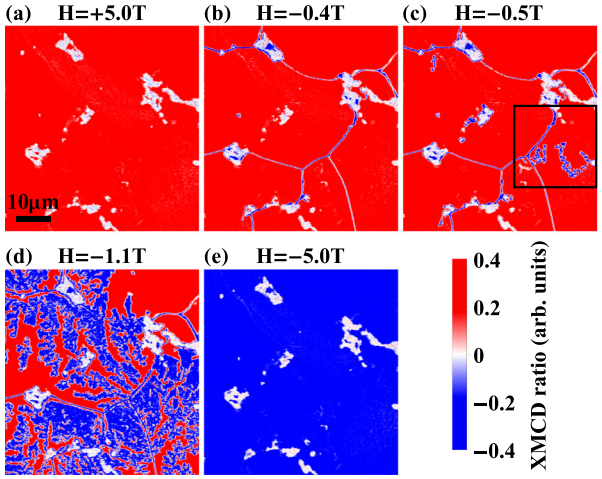

FIG. 2. Co L_3 XMCD maps obtained under external magnetic fields of (a) 5.0 T, (b) −0.4 T, (c) −0.5 T, (d) −1.1 T, and (e) −5.0 T. The black scale shown in (a) was applied to images (b)–(e). The magnetic domain structure denoted by the boxed region in (c) is magnified and shown in Fig. 3.

Composition mapping and line scan measurements of Sm, Co, Fe, Cu, and oxygen were obtained from the intensities of the characteristic x-rays of Sm L_α, Co L, Fe K_α, Cu L, and oxygen K in the energy-dispersive x-ray (EDX) spectrum using a field-emission scanning electron microscope (FE-SEM SU8000, Hitachi High-Technologies Corporation, Tokyo) equipped with an EDX spectrometer (XFlash FlatQUAD 5060F, Bruker Corporation) at an accelerating voltage of 10 keV.

Figure 1 shows the hysteresis curve of $Sm_{0.67}Ce_{0.33}(Co_{0.73}Fe_{0.2}Cu_{0.05}Zr_{0.02})_{7.2}$. The magnetic properties of this magnet are as follows: $B_r = 1.036$ T, $H_{cJ} = 1.47$ T, $H_k = 1.06$ T, and alignment

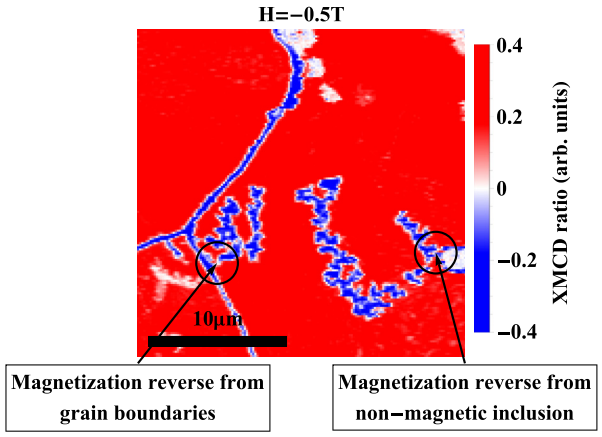

FIG. 3. Magnetic domain structure at a magnetic field of $H = -0.5$ T. The positions where magnetization reversal is initiated from a grain boundary (left circle) and from a nonmagnetic inclusion (right circle) are indicated.

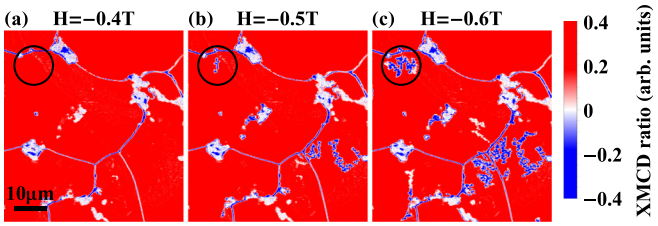

FIG. 4. Magnetization reversal area shown in the circled region generated at neither grain boundaries nor nonmagnetic inclusions in Co L_3 maps: (a) −0.40 T, (b) −0.50 T, and (c) −0.60 T.

$(B_r/J_s) = 0.96$, where J_s is the saturation magnetization measured at a magnetic field of 8 T.

Figures 2(a)–2(e) show Co L_3 edge XMCD maps obtained under external magnetic fields of +5.0 T, −0.4 T, −0.5 T, −1.1 T, and −5.0 T, respectively, where red (blue) indicates that an optical axis component of the Co magnetic moment is parallel (antiparallel) to the axis and white indicates that there is no magnetic moment. Figure 2(a), +5.0 T, shows that the magnetization of every grain (red area) is saturated. White regions correspond to nonmagnetic inclusions or voids. In Fig. 2(b), −0.4 T, the magnetization reversal region (blue) was initiated from the grain boundaries, previously reported using the Kerr effect,[11] and also from the vicinity of the nonmagnetic phases or inclusions. In Fig. 2(c), −0.5 T, the magnetization reversal regions extend to inside the grains from the grain boundaries or nonmagnetic inclusions. When the demagnetization field reached −1.1 T [Fig. 2(d)], the total area of the red region approached that of the blue region and magnetization declined to zero.

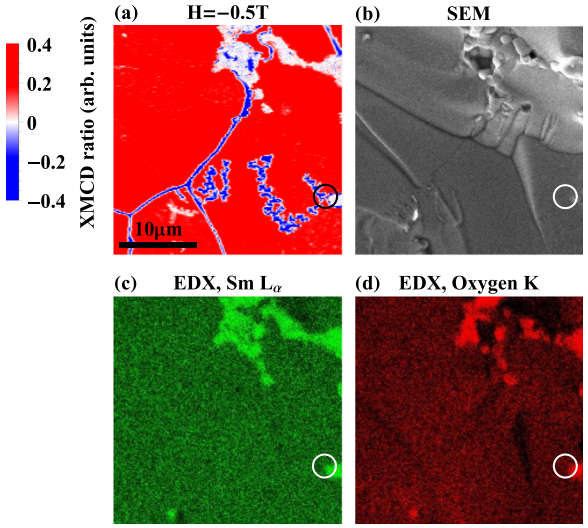

FIG. 5. (a) XMCD map at $H = -0.5$ T, (b) corresponding SEM image, and corresponding EDX maps for (c) Sm and (d) oxygen. The encircled region, where the magnetization reversal occurred and extended into grain, is the Sm oxide.

From the demagnetization curve shown in Fig. 1 and the XMCD maps of Fig. 2, we can see that magnetization reversal occurs only at grain boundaries until near the inflection point of the demagnetization curve or H_k. After the magnetization reversal region extended into the grains, magnetization decreased quickly, eventually reaching coercivity.

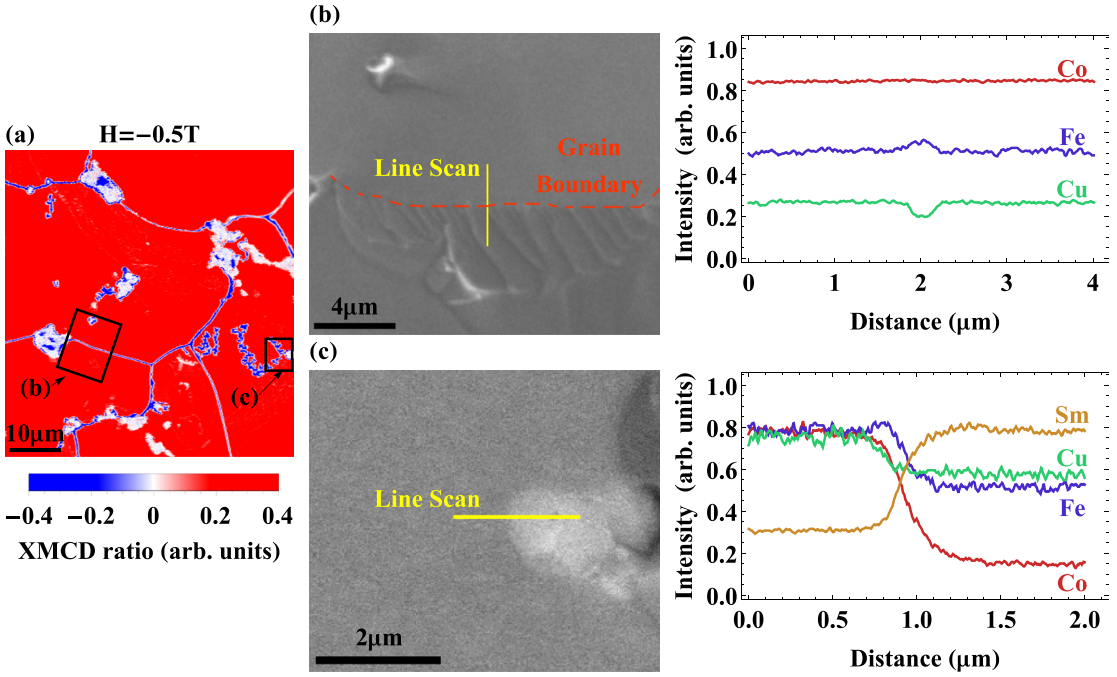

FIG. 6. Co L_3 XMCD map, (a), at $H = -0.5$ T and the results of composition analyses along the lines indicated in (b) and (c). (b) EDX line scan measured across a grain boundary for Cu, Fe, Co, and Sm. (c) EDX line scan measured across a boundary between a grain and a Sm oxide for Co, Fe, Cu, and Sm.

Figure 3 shows an enlarged XMCD map at a magnetic field of −0.5 T. Here, the magnetization reversal region extended into the grains from the grain boundaries and the boundaries of nonmagnetic phases or inclusions. Every magnetization reversal area appearing inside grains comes into contact with the grain boundary and nonmagnetic inclusions as the demagnetization increased. In contrast, Fig. 4 shows some magnetization reversal regions [encircled in Figs. 4(b) and 4(c)] that emerged without coming into contact with the grain boundaries and nonmagnetic inclusions, also noted in previous research.[12,13] Our initial hypothesis is that magnetization reversal might have originated from nucleation or coherent rotation. However, these reversal regions might have originated from grain boundaries or

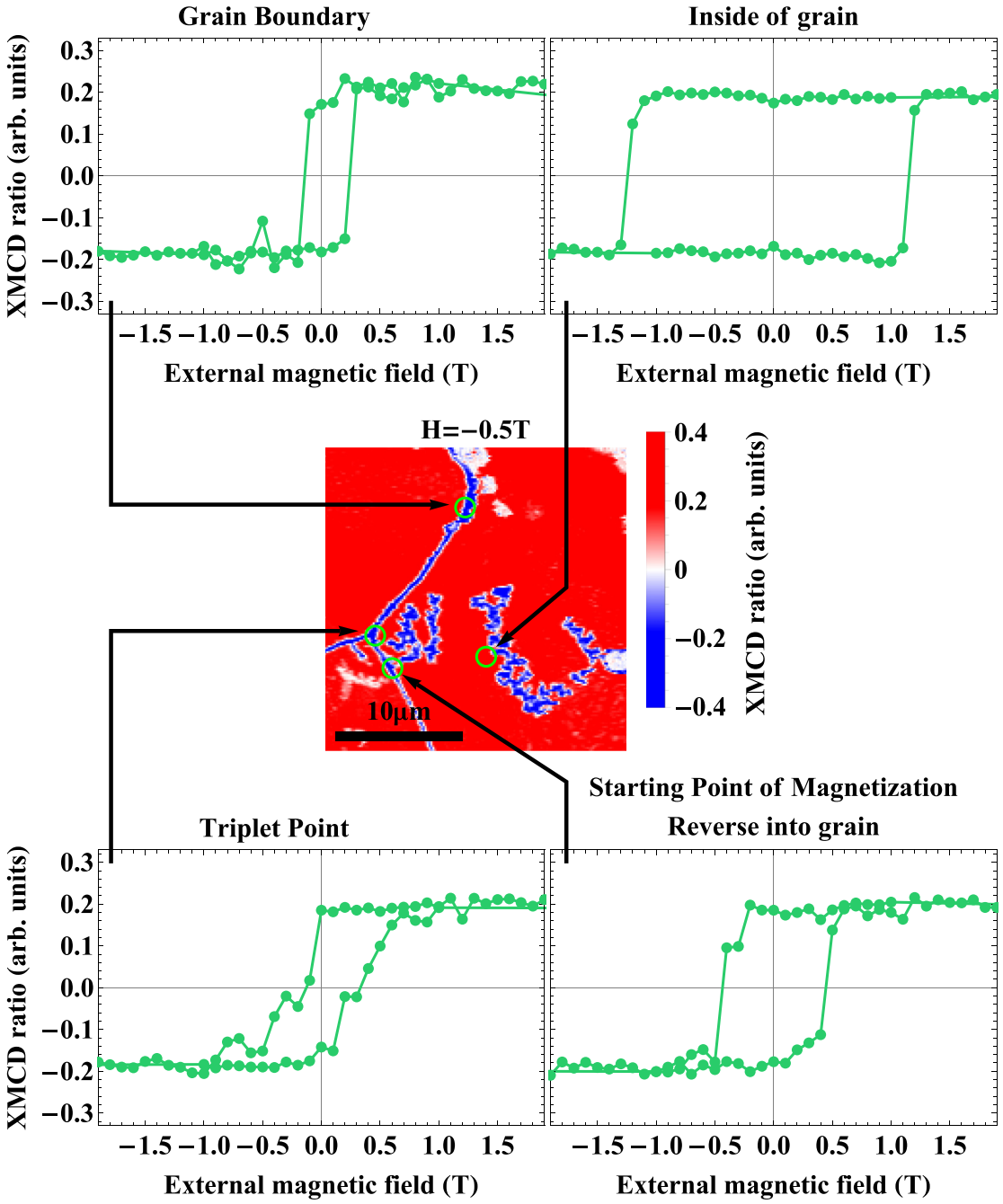

FIG. 7. Local magnetic properties obtained from the Co L_3 XMCD ratio.

nonmagnetic phases underneath the surface and reached the specimen surface via magnetic domain wall motion induced by increasing the applied demagnetization field.

Figure 5(a) shows a Co L_3 XMCD map of $H = -0.5$ T, Fig. 5(b) shows a corresponding SEM image, Fig. 5(c) shows EDX results for Sm, and Fig. 5(d) shows EDX results for oxygen. The EDX maps indicate that the nonmagnetic inclusions inside the grains were Sm oxide.

It would be expected that the composition at the grain boundaries and in the vicinity of the Sm oxide phase inside the grains deviates from that of the grains. To verify this expectation, we obtained SEM images of particular regions within Fig. 6(a), where the first includes two grains and their grain boundary [Fig. 6(b)] and the corresponding EDX line scan for Sm, Co, Fe, and Cu [Fig. 6(b)], and the second shows inside the grain in the vicinity of Sm-oxide [Fig. 6(c)] and the corresponding EDX line scan for Sm, Co, Fe, and Cu. The Fe concentration at the grain boundary was higher than that inside the grain. In contrast, it was found that the Cu concentration at the grain boundary was lower than that inside the grain from the line scan in Fig. 6(b). In the vicinity of Sm oxide, the Co, Fe, and Cu concentration decreased sharply. We hypothesize that these composition variations are responsible for the coercivity drop in these areas.

Figure 7 shows the local magnetic properties evaluated from the Co L_3 edge XMCD signal intensity. The magnetic properties of the grain boundary and the triplet point deteriorated in their coercivities compared to those inside of the grain. The triplet point, which is the junction of the grain boundaries, is expected to have a composition similar to the grain boundaries. It is easy to conjecture that the reverse magnetization area initiated from the grain boundary or from the triplet points.

In conclusion, we investigated magnetization reversal of $Sm_{0.67}Ce_{0.33}(Co_{0.73}Fe_{0.2}Cu_{0.05}Zr_{0.02})_{7.2}$ via XMCD microscopy. The magnetization reversal initially occurs at the grain boundaries or in the vicinity of the Sm oxide inside the grains. When the magnetic field is within the range of -0.4 to -0.5 T, the magnetization reversal domains extend into the grains, where the starting point of magnetization reversal into the grain is shown in Fig. 7. Upon extension into the grains, the reversal domains propagate further into the grains as the reverse magnetic field increases. The Co concentration in the grain boundaries is nearly identical to that inside the grains, whereas the Fe concentration is higher and the Cu concentration is lower at the grain boundaries. We verified that Sm, Co, Fe, and Cu concentrations also differ in the vicinity of Sm oxide phases, indicating that these compositional variations are responsible for the deterioration of coercivity in these regions (where initial magnetization reversal occurs). The local magnetic properties measured by the Co L_3 edge XMCD ratio show that, in these regions, magnetic properties deteriorated in coercivity compared to those inside of the grains.

See the supplementary material for the Sm M_5 XMCD map of the specimen demagnetized at -1.28 T (near the bulk coercivity) after full magnetization at 5 T and measured at zero magnetic field and for the propagation of magnetization reversal with the changing external magnetic field.

This work was supported by the Japan Science and Technology Agency (JST), in part by the Collaborative Research Based on Industrial Demand under Grant No. JPMJSK1617. We thank Shin-Etsu Chemical Co., Ltd. for providing magnet samples. The synchrotron radiation experiments were performed at the BL25SU of SPring-8 with the approval of the Japan Synchrotron Radiation Research Institute (JASRI; Proposal Nos. 2017A1008, 2017B1009, 2018A1010, 2019A1010, and 2019B1153. The XMCD mapping technique used in this work was developed by the Elements Strategy Initiative Center for Magnetic Materials (ESICMM) project with Grant No. JPMXP0112101004, through the Ministry of Education, Culture, Sports, Science, and Technology (MEXT). We thank Edanz Group (www.edanzediting.com/ac) for editing a draft of this manuscript.

DATA AVAILABILITY

The data that support the findings of this study are available from the corresponding author upon reasonable request.

REFERENCES

[1]K. J. Strnat, "Cobalt-rare earth alloys as promising new permanent magnet materials," Cobalt **36**, 133–143 (1967).
[2]G. Hoffer and K. J. Strnat, "Magnetocrystalline anisotropy of YCo_5 and Y_2Co_{17}," IEEE Trans. Magn. **2**, 487–489 (1966).
[3]E. A. Nesbitt, R. H. Willens, R. C. Sherwood, E. Buehler, and J. H. Wernick, "New permanent magnet materials," Appl. Phys. Lett. **12**, 361–362 (1968).
[4]Y. Tawara and H. Senno, "Cerium, cobalt and copper alloy as a permanent magnet material," Jpn. J. Appl. Phys. **7**, 966–967 (1968).
[5]H. Senno and Y. Tawara, "Permanent-magnet properties of Sm-Ce-Co-Fe-Cu alloys with compositions between 1–5 and 2–17," IEEE Trans. Magn. **10**, 313–317 (1974).
[6]T. Ojima, S. Tomizawa, T. Yoneyama, and T. Hori, "Magnetic properties of a new type of rare-earth cobalt magnets $Sm_2(Co, Cu, Fe, M)_{17}$," IEEE Trans. Magn. **13**, 1317–1319 (1977).
[7]Y. Horiuchi, M. Hagiwara, K. Okamoto, T. Kobayashi, M. Endo, T. Kobayashi, T. Nakamura, and S. Sakurada, "Effects of solution treated temperature on the structural and magnetic properties of iron-rich $Sm(CoFeCuZr)_Z$ sintered magnet," IEEE Trans. Magn. **49**, 3221–3224 (2013).
[8]Y. Horiuchi, M. Hagiwara, M. Endo, N. Sanada, and S. Sakurada, "Influence of intermediate-heat treatment on the structure and magnetic properties of iron-rich $Sm(CoFeCuZr)_Z$ sintered magnets," J. Appl. Phys. **117**, 17C704 (2015).
[9]J. D. Livingston and D. L. Martin, "Microstructure of aged $(Co, Cu, Fe)_7Sm$ magnets," J. Appl. Phys. **48**, 1350–1354 (1977).
[10]L. Rabenberg, R. K. Mishra, and G. Thomas, "Microstructures of precipitation-hardened SmCo permanent magnets," J. Appl. Phys. **53**, 2389–2391 (1982).
[11]H. Machida, T. Fujiwara, R. Kamada, Y. Morimoto, and M. Takezawa, "The high squareness Sm-Co magnet having $H_{cb} = 10.6$ kOe at 150 °C," AIP Adv. **7**, 056223 (2017).
[12]H. Machida, T. Fujiwara, C. Fujimoto, Y. Kanamori, J. Tanaka, and M. Takezawa, "Magnetic domain structures and magnetic properties of lightly Nd-doped Sm-Co magnets with high squareness and high heat resistance," IEEE Trans. Magn. **55**, 1–4 (2019).
[13]H. Machida, T. Fujiwara, C. Fujimoto, Y. Kanamori, K. Sakakura, and M. Takezawa, "Magnetic properties and microstructures of high heat-resistance Sm-Co magnets with high Fe and low Zr content," AIP Adv. **9**, 125042 (2019).
[14]Y. Kotani, Y. Senba, K. Toyoki, D. Billington, H. Okazaki, A. Yasui, W. Ueno, H. Ohashi, S. Hirosawa, Y. Shiratsuchi, and T. Nakamura, "Realization of a scanning soft x-ray microscope for magnetic imaging under high magnetic fields," J. Synchrotron Radiat. **25**, 1444–1449 (2018).
[15]D. Billington, K. Toyoki, H. Okazaki, Y. Kotani, T. Fukagawa, T. Nishiuchi, S. Hirosawa, and T. Nakamura, "Unmasking the interior magnetic domain structure and evolution in Nd-Fe-B sintered magnets through high-field magnetic imaging of the fractured surface," Phys. Rev. Mater. **2**, 104413 (2018).